This project has received funding from the European Union's Horizon 2020 research and innovation programme under grant agreement No 871813.

MUNDFAB

ICT Project No 871813

MUNDFAB

Modeling Unconventional Nanoscaled Device FABrication

D4.7: Complete model for alloy redistribution and doping, calibrated with the second round of experiments

D. Ricciarelli (CNR), A. La Magna (CNR), G. Calogero (CNR), I. Deretzis (CNR), G. Fisicaro (CNR), R. Daubriac (CNRS), R. Demoulin (CNRS), F. Cristiano (CNRS), J. Müller (CNRS), G. Larrieu (CNRS), B. Sklénard (CEA), S. Kerdiles (CEA), M. Opprecht (CEA), J.-M. Hartmann (CEA)

December 19, 2022

Fraunhofer IISB leti ceatech cnrs Łukasiewicz Instytut Technologii Materiałów Elektronicznych life.augmented TU WIEN

Quality management

This deliverable was reviewed by:

Diego Milardovich, TUW

Simon Mundinar, Fraunhofer

Contents

Executive Summary

This document reports on a functioning model for the process of melting and alloy redistribution of $Si_{1-x}Ge_x$. A calibration of the dielectric functions of l-$Si_{1-x}Ge_x$, which is essential to reproduce the evolution of the melting front upon laser irradiation, is delivered with an indirect approach, employing data of relaxed samples from the second round of experiments. The calibration is further tested on experimental data for strained thin samples. The model of $Si_{1-x}Ge_x$ is extended to pattern structures with simplified two-dimensional approaches. These samples were prepared by CNRS, as reported in deliverable D4.6, and will be irradiated by CEA in the remaining part of WP4 experiments. Deliverable D4.7 can be considered as a premise for the final deliverable dedicated to modeling in WP4 (i.e., deliverable D4.8). As indicated in other project documents, the calibration of the $Si_{1-x}Ge_x$ alloy is *per se* a difficult task and merits a dedicated report.

1. Introduction

Laser annealing (LA) with pulsed power emission (pulse duration below 10^{-6} s) can be integrated in thermal processes for micro- and nano-electronics, yielding versatile and powerful solutions in extremely constrained space and time scales. The employment of the laser enables the melting of well define regions at the nanoscale with the advantages of a better control of the junction and a higher dopant activation efficiency if compared to the conventional rapid thermal annealing. The dopant atoms redistribute uniformly due to the high diffusivity (10^{-4} cm^2/s in the liquid phase). Moreover, the nonequilibrium segregation during the fast solidification enhances dopant trapping and favors the incorporation of a high density of dopant atoms in substitutional positions. These processes occur in a tiny time window of few ns, depending on the different laser pulse duration. Thanks to these particular characteristics, laser annealing is nowadays widely applied as a post-fabrication annealing step to activate isolated doped regions with a limited heating of the other zones of the devices. [1, 2]. Optimal control is a key issue for the successful application of LA during a thermal process workflow. Due to the specificity of the electromagnetic energy absorption and the ultra-rapid thermal diffusion of the LA process, the potential benefits of LA require a process design, which is unique in microelectronics, and is complementary to the device design. This complexity impacts on the Design of Experiments (DoE) for the optimization of LA processes. Within this context, reliable simulations of LA are required for optimizing the process parameters while reducing the number of experimental tests, with the help of a virtual DoE. The MUNDFAB project deals with the advanced TCAD of processes characterized by a low thermal budget, dedicating WP4 to the simulation of LA. Among the various issues considered in WP4, a critical one is the calibration of material parameters, which is fundamental to achieve the full predictivity of the models. In derivable D4.1, a systematic categorization of the physical parameters, required for the successful simulation of LA processes, has been reported for several materials commonly employed in microelectronic devices. Critical issues with respect to parameter calibration were also identified, with $Si_{1-x}Ge_x$ alloys showing a high level of difficulty due to the non-definite nature of their lattice and the dependence of the optical parameters on the alloy fraction and dopant concentration. Deliverable D4.2 reported on experimental measurements that were performed for the extraction of the optical constants of solid $Si_{1-x}Ge_x$ at different temperatures (in the range from room temperature to 873 K, i.e., well below the melting threshold), stoichiometries and dopant concentrations. These results were used for the derivation and calibration of semiempirical functions that can be applied within the LA simulation workflow. Based on this scheme, LA process simulations were performed by existing custom research tools at CNR and CEA institutes. We notice that these tools rely on a continuum method solving coupled Partial Differential Equations (PDEs) which rule the evolution of the “evolving fields” during the pulsed irradiation (e.g., electromagnetic field, temperature, phase, alloy fraction, dopant density, etc), whereas innovative atomistic models were also developed from scratch within the MUNDFAB project (see deliverable D4.4). Considering the continuum models, the melting process is simulated with a phase field approach, where the presence of the liquid is considered with this additional field whom takes a value of 0 for the liquid and a value of 1 for the crystal phases. The evolution of the latter is governed by a diffusion interface equation [3].

Preliminary results based on this continuum model, with upgraded calibration, have been reported in deliverable D4.4 and were compared with experimental SIMS measurements of LA processed strained $Si_{1-x}Ge_x$/Si structures (i.e., ~30 nm $Si_{1-x}Ge_x$ thin films deposited by chemical

vapor deposition on Si substrates). The quality of the calibration of solid $Si_{1-x}Ge_x$ dielectric functions has been demonstrated by comparing the predicted laser melt threshold, i.e., the lower laser energy density necessary to melt the material, with experimental data.

Data from the first round of experiments, reporting on strained thin $Si_{1-x}Ge_x$ samples (as thin as ~30 nm), allowed an introductory study of the laser-matter interaction with $Si_{1-x}Ge_x$. However, the extremely small thickness of the considered samples and the underlying Si substrate (with completely different thermal parameters) makes it unsuitable for a correct validation of thermal energy evolution. Moreover, the previous calibration of the liquid $Si_{1-x}Ge_x$ (l-$Si_{1-x}Ge_x$) permittivity function, ϵ, was based on a first order linear combination of the liquid Si and Ge ϵ values, which are temperature independent. This choice was also motivated by the limited number of investigated cases in the first round of experiments, restricted only to $Si_{1-x}Ge_x$ thin films, and, consequently, by the difficulty in getting possible dependencies of the l-$Si_{1-x}Ge_x$ ϵ on the liquid phase temperature $T_{l\text{-}SiGe}$ and on higher order X_{Ge} terms.

The second round of experiments (see deliverable D4.6) extends the existing datasets with thick $Si_{1-x}Ge_x$ relaxed layers and can be exploited to overcome the aforementioned limitations. In the reported cases the evolution of the thermal field is governed by the alloy fraction of $Si_{1-x}Ge_x$ as phonon scattering hinders the thermal conduction [4]. The use of relaxed thick samples impacts the melting thresholds, leading to significantly smaller values with respect to strained $Si_{1-x}Ge_x$ (see deliverable D4.6). Moreover, the extension of the melting process to relatively large $Si_{1-x}Ge_x$ regions with constant value of X_{Ge} allows the evaluation of cases where the melt depth overcomes ~ 100 nm. These experimental results are sensitive on the alloy fraction of the optical parameters and indirectly also on temperature effects that are controlled by the different energy density of the laser radiation. These data enable an indirect calibration of l-$Si_{1-x}Ge_x$ real (Re ϵ_{l-SiGe}) and imaginary (Im ϵ_{l-SiGe}) dielectric functions via a comparison of experimental and simulated melt depths.

In our study, we discuss a complete calibration of the optical properties of l-$Si_{1-x}Ge_x$, based on this second round of experiments employing blanket samples, i.e., without silicon dioxide (SiO_2) substrate. We present the results of this model in predicting the LA process in patterned samples that have been fabricated (see deliverable D4.6) and which will be irradiated in the remaining experimental activity of WP4. The report is organized as follows: section 2 deals with the calibration of the optical constants of l-$Si_{1-x}Ge_x$ with the available experimental data on relaxed samples, section 3 is dedicated to the validation of the resulting model with previous LA experiments on strained thin samples, section 4 is devoted to the results of laser annealing simulations on $Si_{1-x}Ge_x$ patterned structures and, finally, conclusions are drawn in section 5.

2. Calibration of the optical constants of l-$Si_{1-x}Ge_x$

LA simulations were performed using the continuum approach mentioned in the introduction with Ge profiles of relaxed thick $Si_{1-x}Ge_x$ samples taken from the second round of experiments (see deliverable D4.6). As shown in Figure 2.1, these profiles are characterized by a region of constant alloy fraction with a length of more than 1000 nm. According to the experimental dataset, two different alloy fractions were considered, i.e., 0.24 and 0.58. Motivated by the isotropic distribution of the melt in the experiments, with almost negligible morphological effects, we use a simple mono-dimensional mesh, reported in Figure 2.1. This prototype

presents a total length of 4500 nm and is divided into three different portions, with a progressively increased mesh grain, from a minimum of 0.5 nm to a maximum of 5 nm. These regions are divided as follows, (i) the $Si_{1-x}Ge_x$ region, 1300 nm long with a constant alloy fraction, (ii) the $Si_{1-x}Ge_x$ graded region with a length of 2500 nm and variable X gradually decaying to X=0 and (iii) the pure Si region, 700 nm long. The time harmonic electromagnetic field, computed from Maxwell equations, mimics the same characteristics of the laser employed at CEA, with a wavelength of 308 nm and a pulse time of 160 ns. We further consider different energy densities (ED), i.e., laser fluencies, of the radiation.

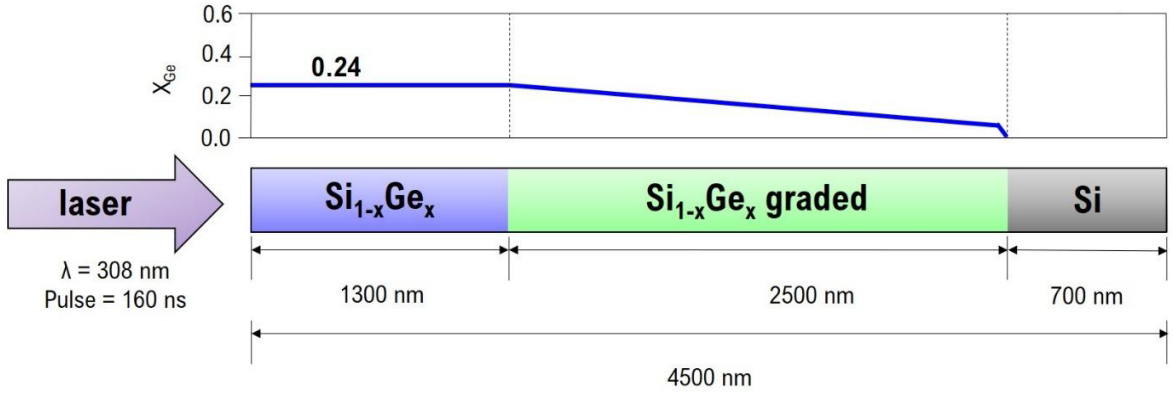

***Figure 2.1**: Schematic of the mono-dimensional model employed for laser annealing simulations on relaxed $Si_{1-x}Ge_x$ samples: defined regions of the sample and initial (time = 0 ns) alloy fraction profile for X_{Ge}=0.24.*

A preliminary approximation for the l-$Si_{1-x}Ge_x$ dielectric constant, ϵ_{l-SiGe}, consists in a linear combination of the dielectric constant of the Si and Ge elements weighted by the respective molar fractions (1).

$$\epsilon_{l-SiGe}(X_{Ge}) = \epsilon_{l-Ge} \cdot X_{Ge} + \epsilon_{l-Si} \cdot (1 - X_{Ge}) \quad (1)$$

This approximation is reliable for an almost ideal binary system where Si and Ge are fully miscible in the whole range of composition. However, it neglects effects related to second and third order terms of the Ge concentration, arising from the interaction of Si and Ge in the liquid alloy and, further, it fails to reproduce possible temperature effects. To the best of our knowledge, the real and imaginary dielectric constants of l-Si and l-Ge, reported in Table 2.1, are independent, or at least scarcely dependent, on the temperature of the liquid [5-8]. The interpolation between the physical properties of Si and Ge, expressed in (1), represents a starting point for the calibration of the material.

***Table 2.1.** Real (Re) and imaginary (Im) permittivity of l-Si and l-Ge. [7, 8]*

	ϵ_{l-Ge}	ϵ_{l-Si}
Re	-14.585	-15.734
Im	9.517	10.126

The use of the linear combinations for Re and Im ϵ_{l-SiGe} in the laser annealing simulations, delivers some inconsistency between the simulated melt depths (MD) and the experimental

ones, as shown in Table 2.2 (see melt depth values for original Im ϵ_{l-SiGe}) and Figure 2.3. The error bar of the computed MD depends on the energy density of the laser. We found that for ED ≤ 1.10 J cm^{-2} the melt depth is overestimated by more than ~ 17 nm, while a good agreement is retrieved for higher EDs, as for ED ~ 1.50 J cm^{-2}.

Table 2.2. *Melt depths obtained by using the original linear combination model of l-Si$_{1-x}$Ge$_x$ dielectric functions (Original Im ϵ_{l-SiGe}) and by the study of the Im ϵ_{l-SiGe} variation (Varied Im ϵ_{l-SiGe}) for a laser pulse of 160 ns. Experimental values are taken from deliverable D4.6.*

Melt Depth Relaxed Si$_{1-x}$Ge$_x$ vs Im $\epsilon_{l-Si_{1-x}Ge_x}$									
		Exp.	**Original Im. ϵ l-SiGe**			**Varied Im. ϵ l-SiGe**			
X_{Ge}	**ED [J cm^{-2}]**	**Melt Depth [nm]**	**Im ϵ l-SiGe**	**R l-SiGe**	**Melt Depth [nm]**	**Im ϵ l-SiGe**	**R l-SiGe**	**T_{l-SiGe} [K]**	**Melt Depth [nm]**
0.24	0.75	25	9.98	0.778	42	7.50	0.815	1642	24
0.24	0.80	26	9.98	0.778	54	6.50	0.833	1643	24
0.24	1.10	100	9.98	0.778	132	8.00	0.806	1647	99
0.24	1.50	238	9.98	0.778	243	10.00	0.777	1681	243
0.58	0.90	74	9.77	0.780	105	7.50	0.809	1560	84
0.58	1.50	294	9.77	0.780	285	10.00	0.772	1609	287

The aforementioned discrepancies can be explained considering the reflectivity of the melt. Reflectivity is linked to the real and imaginary dielectric functions by the expressions (2)-(4), via the real, n, and imaginary, k, refractive indices.

$$n = \sqrt{\frac{Re\,\epsilon + \sqrt{(Re\,\epsilon)^2 + (Im\,\epsilon)^2}}{2}} \quad (2)$$

$$k = \frac{Im(\epsilon)}{2n} \quad (3)$$

$$R = \frac{(n-1)^2 + k^2}{(n+1)^2 + k^2} \quad (4)$$

As shown in Table 2.2 (Original Im ϵ_{l-SiGe}), expressing the dielectric constant of l-Si$_{1-x}$Ge$_x$ as a simple linear combination of the single elements provides almost identical reflectivity values of the melt, i.e., 0.78 for different germanium concentrations and temperatures. However, this might not be the case for the region of X_{Ge} located far from the upper and lower bounds. We investigated this aspect, by studying the dependency of the MD on the imaginary dielectric function value. To this regard Im ϵ_{l-SiGe} becomes a hyper-parameter that links the optical constants of l-Si$_{1-x}$Ge$_x$ to melt depths and allows an extension of the previous calibration. We

found optimal values of Im ϵ_{l-SiGe}, reported in Table 2.2 (see Varied Im ϵ_{l-SiGe} section), for which the obtained MDs are comparable to the experiment. T_{l-SiGe} temperatures reported in Table 2.2 correspond to the air-liquid interface. As a matter of fact, the radiation extinguishes within the first nanometers of the irradiated sample. Quantitatively, a calculated complex refractive index of 4.11 for X_{Ge}=0.24 delivers an extinction coefficient (5) of 0.1678 nm^{-1}, with a resulting absorption length of ~ 6 nm.

$$\alpha = \frac{4\pi k}{\lambda} \quad (5)$$

Results collected with this approach help us to understand the effective dependence of the optical parameters on the temperature and alloy fraction. If we focus on data with X_{Ge} = 0.24, we observe that optimal l-$Si_{1-x}Ge_x$ reflectivities up to ~ 0.83 are required for T_{l-SiGe} near the melting point, while values of ~ 0.78, identical to those arising from the original model, are required for T_{l-SiGe}> 1680 K. An almost identical behavior is observed for X_{Ge} = 0.58, despite the availability of only two experimental points.

With this analysis in mind, we elaborated an extension of expression (1), accounting for the optical behavior of the melt for T_{l-SiGe} near $T_{m\text{-}SiGe}$, corresponding to the region located on the liquidus line or few kelvins above the melting point. Accordingly, we replaced X_{Ge} in (1) with $f(X_{Ge}, T_{l-SiGe})$, a function which is cubic on X_{Ge} and linear on T_{l-SiGe}. The cubic dependency on the germanium fraction X_{Ge} is needed to effectively reproduce, at the same time, the pure elements boundaries X_{Ge}= 0 and X_{Ge}= 1, and the values of the dielectric function at X_{Ge}= 0.24 and X_{Ge}= 0.58, as a matter of fact previous attempts with a quadratic dependency leads to an inexact reproduction of the function at the points employed for the fitting. Furthermore, the temperature dependency has been tested for selective cases and we found only marginal impact of higher order T_{l-SiGe} terms in reproducing the experimental melt depths of these relaxed samples. The function $\epsilon_{l-SiGe}(T_{l-SiGe}, X_{Ge})$ is detailed by expressions (6)-(8).

$$\epsilon_{l-SiGe}(T_{l-SiGe}, X_{Ge}) = \epsilon_{l-Ge} \cdot f(T_{l-SiGe}, X_{Ge}) + \epsilon_{l-Si} \cdot [1 - f(T_{l-SiGe}, X_{Ge})] \quad (6)$$

$$f(X, T) = g_1(T_{l-SiGe}) \cdot X_{Ge}^3 + g_2(T_{l-SiGe}) \cdot X_{Ge}^2 + [1 - g_1(T_{l-SiGe}) - g_2(T_{l-SiGe})] \cdot X_{Ge} \quad (7)$$

$$g_i(T) = a_i(T_{l-SiGe} - T_{mGe}) + b_i \quad (8)$$

a_i and b_i are parameters determined by the fitting of the optimal Im. ϵ_{l-SiGe} value reported in Table 2.2 vs the X_{Ge} and T_{l-SiGe} variables. The conditions $f(0,T)$ = 0 and $f(1,T)$ = 1 define the lower and upper bounds corresponding to l-Si and l-Ge respectively. The obtained fitting parameters are reported in Table 2.3 and an extended reflectivity map of $Si_{1-x}Ge_x$ for a wavelength of 308 nm is shown in Figure 2.2.

Table 2.3. *Calibrated parameters for the real and imaginary permittivity of $Si_{1-x}Ge_x$ alloys.*

$\epsilon_{l-SiGe}(T,X)$ **fitting parameters**						
	ϵ_{l-Ge}	ϵ_{l-Si}	a_1 [K^{-1}]	b_1	a_2 [K^{-1}]	b_2
Real	-14.585	-15.734	-	-	-	-
Imaginary	9.517	10.126	1.157	$-6.423 \cdot 10^2$	$-5.131 \cdot 10^{-1}$	$3.205 \cdot 10^2$

The map (see Figure 2.2) summarizes two major points of our analysis, (i) the liquidus reflectivity is maximized for X_{Ge}~ 0.5 and (ii) by increasing the temperature, it decays to a constant value of ~ 0.78. A possible reason behind these results relies on the different nature of the various Si-Ge bonds in the liquid if compared to Si-Si and Ge-Ge ones. There might be a concentration-temperature dependent interplay between covalent and metallic bonds that deserves further investigations.

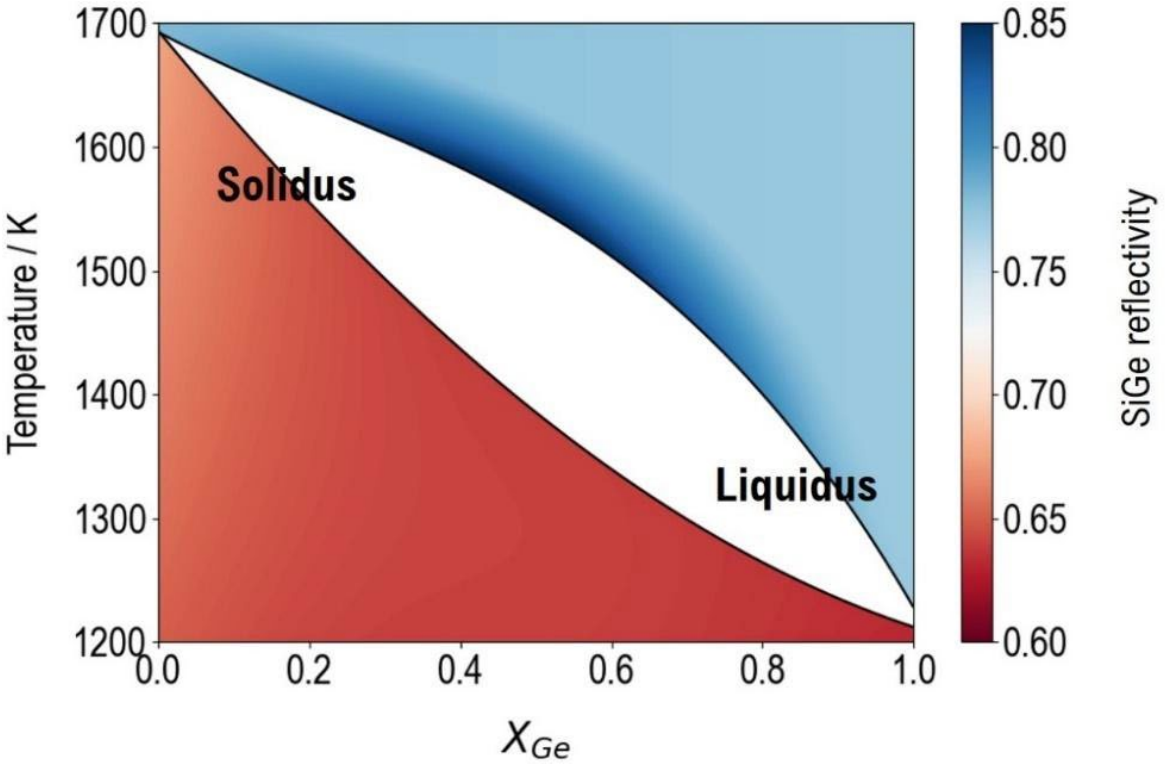

Figure 2.2: *Reflectivity map of $Si_{1-x}Ge_x$ at 308 nm as a function of temperature and alloy fraction.*

Notably, the model gives rise to a great overlap between the simulated and experimental Ge profiles, as shown in Figure 2.3c-d.

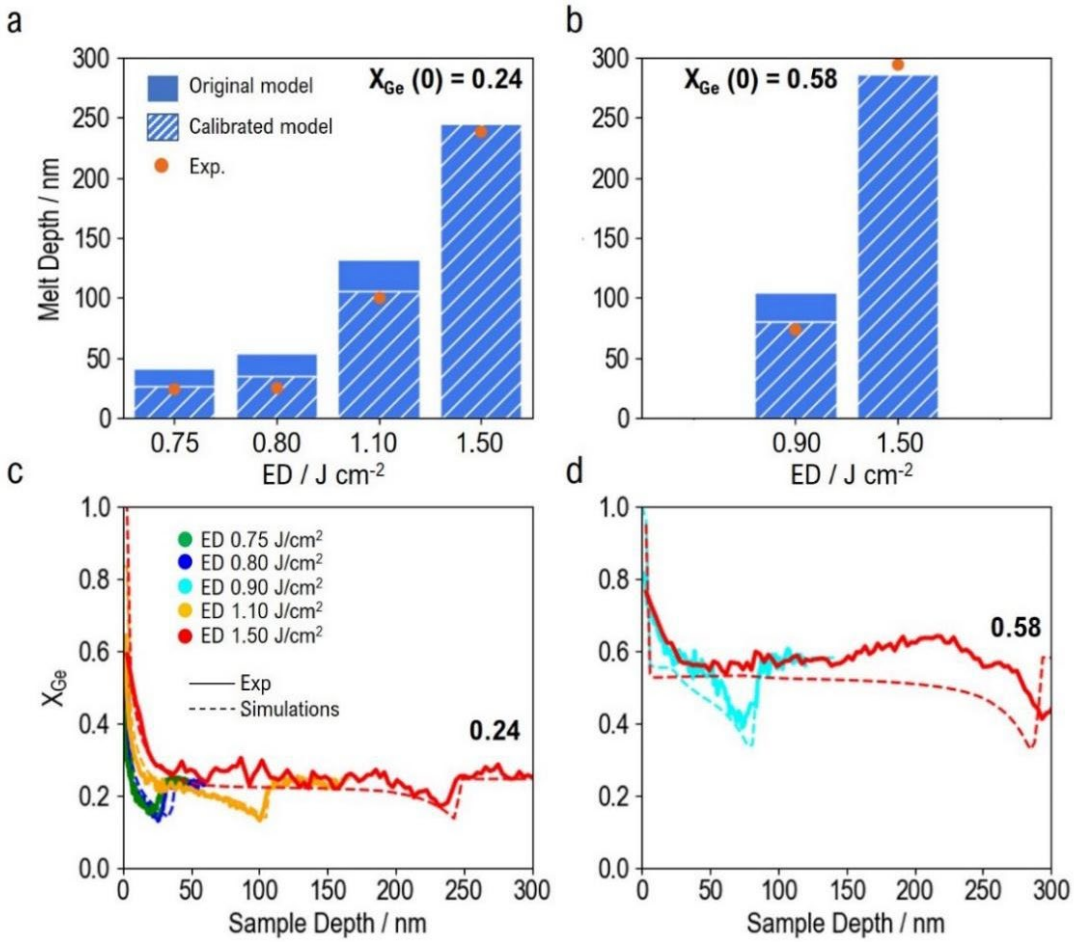

Figure 2.3: *Comparison between experimental and simulated MD for relaxed $Si_{1-x}Ge_x$ samples with initial alloy fractions of 0.24 (a) and 0.58 (b). Comparison between experimental and simulated Ge profile for relaxed $Si_{1-x}Ge_x$ samples with initial alloy fractions of 0.24 (c) and 0.58 (d).*

3. Validation of the model with strained samples

We extend our modeling to strained $Si_{1-x}Ge_x$ samples. The model used for this purpose is identical to the previous one, with the difference of the initial alloy profile, characterized by only 30 nm of $Si_{1-x}Ge_x$, followed by a sharp $Si_{1-x}Ge_x$/Si interface of 1 nm and by 4470 nm of Si (see Figure 3.1). We benchmarked our results to previous experiments published in Refs [7, 9, 10] and to measurements provided in deliverable D4.2 by Ł-IMiF.

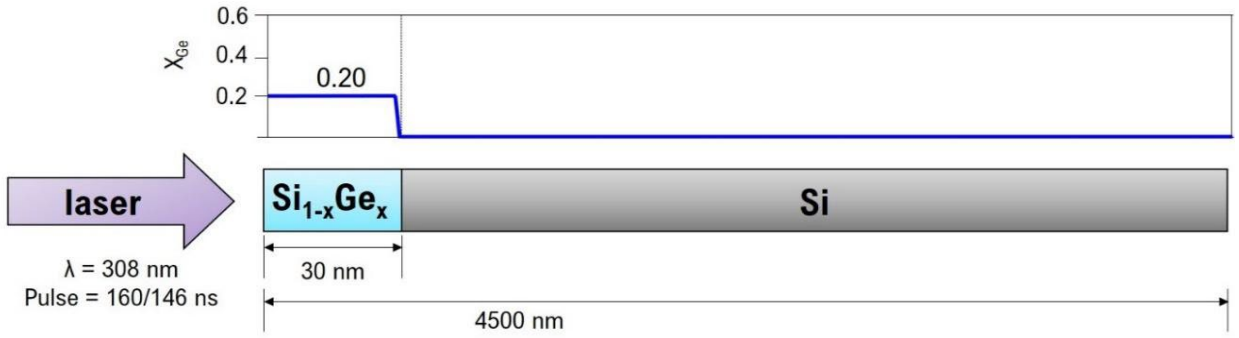

Figure 3.1. *Scheme of the mono-dimensional model used for LA simulations of strained $Si_{1-x}Ge_x$ samples: defined regions of the sample and initial (time = 0 ns) alloy fraction profiles.*

Table 3.1 *Melt depths obtained for $Si_{1-x}Ge_x$ strained samples with the different calibrations. *In these cases, the liquid front overcomes the 30 nm of strained $Si_{1-x}Ge_x$.*

Melt Depth Strained $Si_{1-x}Ge_x$ vs R_{l-SiGe}										
			Exp.		**Original Im. ϵ I-SiGe**			**Calibrated Im. ϵ I-SiGe**		
X	**ED**	**Pulse**	**Melt Depth**	**Ref.**	R **I-SiGe**	**T_{I-SiGe}**	**Melt Depth**	R **I-SiGe**	**T_{I-SiGe}**	**Melt Depth**
	[J cm^{-2}]	**[ns]**	**[nm]**			**[K]**	**[nm]**		**[K]**	**[nm]**
0.20	1.80	146	13	[10]	0.778	1654	20	0.803	1653	13
0.20	2.00	146	21	[10]	0.778	1703	47	0.802	1655	27
0.20	2.20	146	37	[10]	0.778	1736	81*	0.778	1730	74*
0.40	1.60	146	8	[9]	0.776	1609	12	0.819	1610	9
0.40	1.81	146	16	[9]	0.776	1611	29	0.819	1610	13
0.40	2.00	146	27	[9]	0.776	1705	47	0.819	1609	25
0.40	2.20	146	37	[9]	0.776	1735	88*	0.776	1717	64*
0.20	1.80	160	13	[7]	0.778	1651	14	0.807	1650	10
0.20	2.00	160	23	[7]	0.778	1703	47	0.805	1651	18
0.20	2.20	160	41	[7]	0.778	1736	88*	0.778	1710	53*
0.30	1.60	160	7	D4.2	0.777	1650	7	0.812	1635	7
0.30	1.95	160	22	D4.2	0.777	1655	29	0.815	1632	16
0.30	2.20	160	48	D4.2	0.777	1713	68*	0.777	1701	49*

Three different Ge mole fractions of 0.20, 0.30 and 0.40 and two different laser pulses of 160 ns and 146 ns were considered. Our results, reported in Table 3.1 and Figure 3.2, confirm that the temperature/alloy fraction dependence on the optical constant is key to achieve a reasonable agreement with the experiment. In contrast, the temperature independent model predicts melt depths > 16 nm. Figure 3.2 shows a good overlap of the Ge profiles for alloy concentrations of 0.4 and 0.2 and a laser pulse of 146 ns.

Despite our calculations yielding errors of few nm, it is important to report the existence of particular cases, highlighted in Table 3.1, where, due to the high energy densities (ED = 2.20 J cm^{-2}), the liquid front surpasses the 30 nm of strained $Si_{1-x}Ge_x$ samples, entering the pure Si region. For these conditions, we obtained MD errors > 37 nm (see Figure 3.2 and Table 3.1). We notice that this effect is maximized for laser pulses of 146 ns and can be suppressed only by increasing the l-$Si_{1-x}Ge_x$ reflectivity to ~ 0.80.

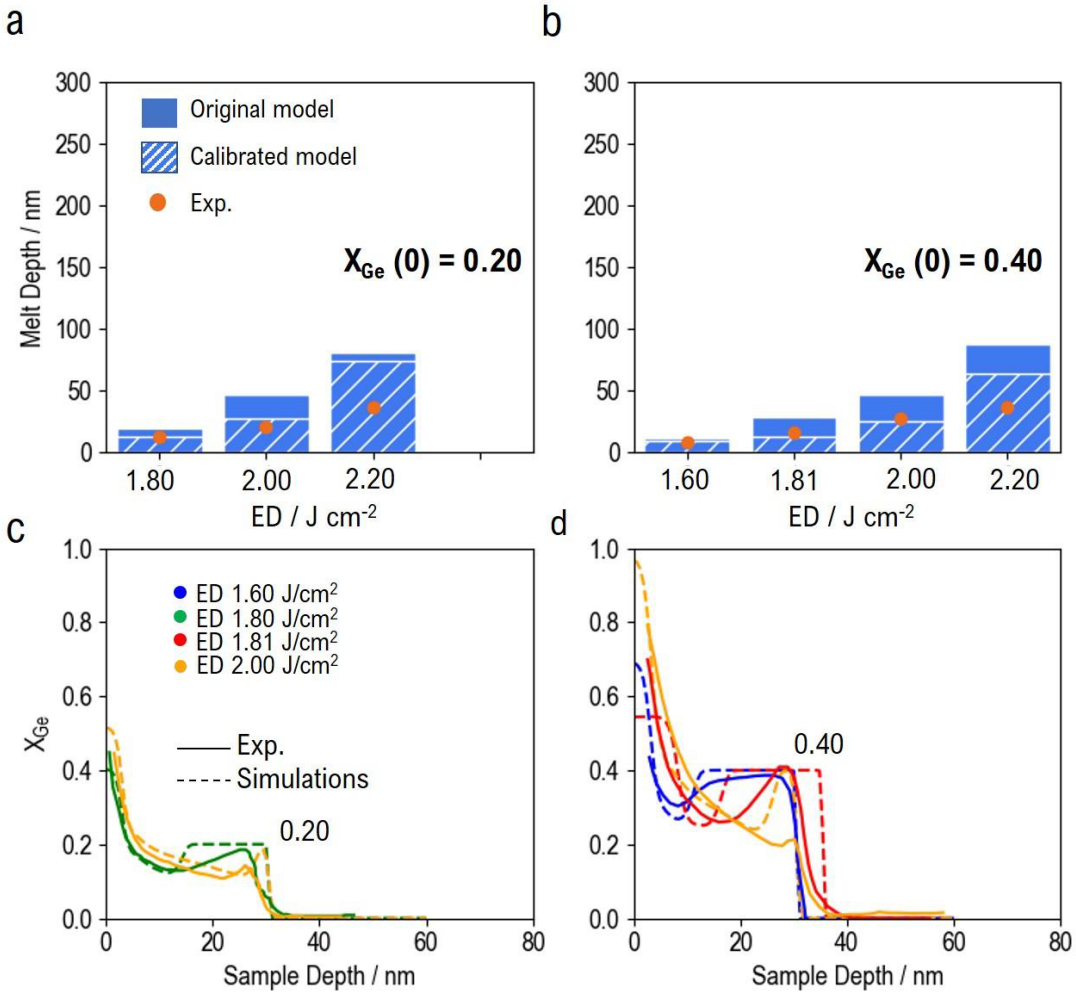

Figure 3.2: *Comparison between experimental and simulated MDs for strained $Si_{1-x}Ge_x$ samples with initial X_{Ge} concentration of 0.20 (a) and 0.40 (b), 308 nm irradiation wavelength and 146 ns of laser pulse. Comparison between experimental and simulated Ge profile for strained $Si_{1-x}Ge_x$ samples with initial X_{Ge} concentration of 0.20 (c) and 0.40 (d).*

4. Simulation of $Si_{1-x}Ge_X$ pattern structures with two-dimensional models

The model is further extended to $Si_{1-x}Ge_x$ pattern structures. The corresponding samples were fabricated at CNRS and will be further irradiated at CEA in the remaining part of WP4 experiments. We notice that different geometries and structure patterns change the way electromagnetic waves are adsorbed and, consequently, the interaction with the sample is different. Hence, it is important to consider not only the effect of laser energy densities (mono-dimensional case), but also the mutual interdependence between geometric effects and optical

parameters. Light polarization can be also selected as a process parameter in the industrial laser tools.

We model $Si_{1-x}Ge_x$ pattern structures with a simplified two-dimensional (2D) model, schematized in Figure 4.1. This considers the relaxed thick $Si_{1-x}Ge_x$ structure capped with SiO_2. The density of the SiO_2 lines in our modeling is controlled by the width (W) and pitch (P) parameters, describing the mutual spacing between different SiO_2 layers. Our 2D model (see Figure 4.1) is composed by a SiO_2 slab with a height of 50 nm and a variable width (W), and a $Si_{1-x}Ge_x$ + Si bottom layer similar to the one introduced in Figure 2.1, with a base corresponding to the pitch value (P). The laser used for our simulations presents a wavelength of 308 nm and a pulse of 160 ns. For our study, we consider combinations of W and P that represent limited cases for stable structures tested in D4.6 by CNRS. Specifically, we employ W values of 30 nm and 80 nm and P values of 120 nm and 200 nm. Two initial alloy fractions were considered following D4.6, i.e., X_{Ge}= 0.204 and X_{Ge}= 0.507.

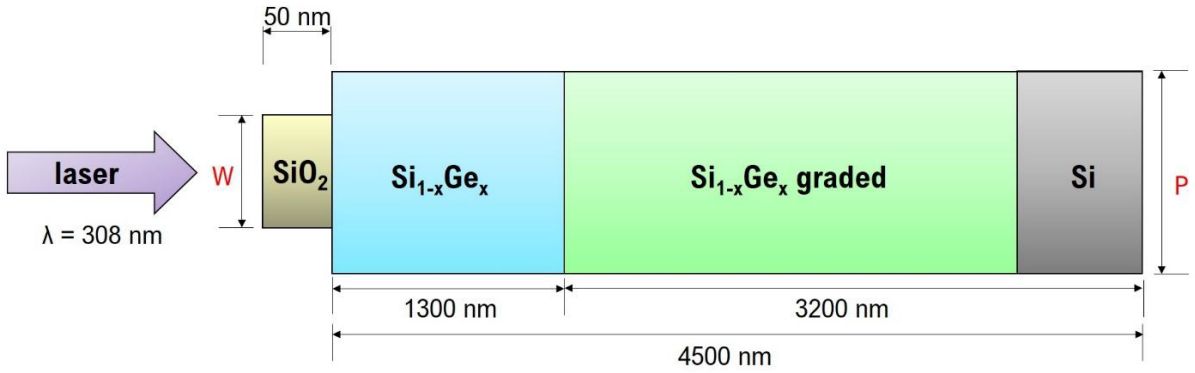

Figure 4.1: *Schematic of the 2D model employed for LA simulations on $Si_{1-x}Ge_x$ patterned structures.*

The evolution of most of the physical fields during the melting process is reported in Figure 4.2. From Figure 4.2a, we observe a slight alteration of the electromagnetic field module due to the diffraction induced by the SiO_2 capping layer, this is more evident in the snapshot shown in Figure 4.3 captured at 110 ns. We notice that the temperature field (Figure 4.2b), phase fields (Figure 4.2c) and alloy fraction (Figure 4.2d) evolve after the melting with an isotropic distribution, as occurs in the mono-dimensional analogues, in spite to the 2D distribution of the temperature field in the heating stage. This feature is due to the capillarity effect and tight space periodicity of the patterning with nanoscale range of the pitch size. The melting thresholds, reported in Table 4.1, present an anti-reflectivity behavior with respect to the value of the blanket, i.e., W = 0 nm. For a fixed pitch of 120 nm, the values are smaller than the blanket of ~ 0.05 / ~ 0.10 J cm^{-2}, while they remain unaltered in W. On the other hand, for a fixed P of 200 nm, ED threshold values are slightly reduced by increasing the capping layer size.

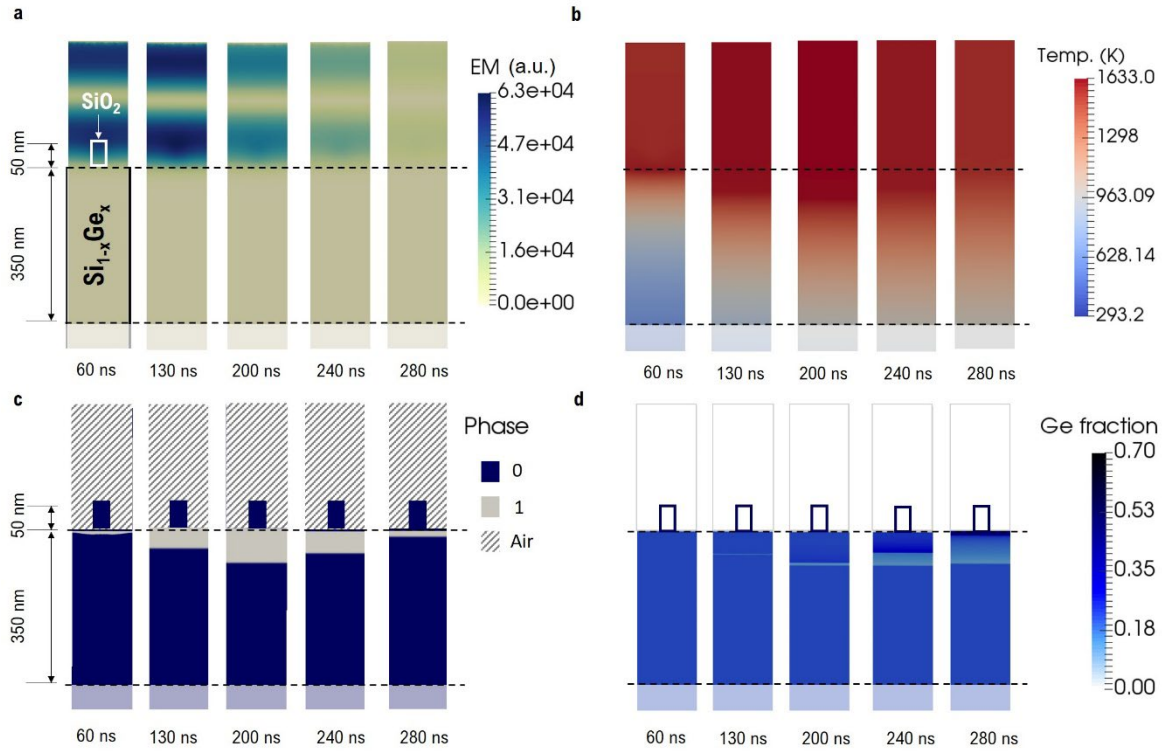

Figure 4.2: *Representation of the evolution of key physical fields in the LA process of $Si_{1-x}Ge_x$ patterned structures with snapshots at 60, 130, 200 (maximum MD), 240 and 280 ns. Images refer to a laser irradiated sample with an ED of 0.8 J cm^{-2}, a width (W) of 30 nm and a pitch (P) of 120 nm and an initial alloy fraction of 0.2. (a) Electromagnetic field module, (b) temperature, (c) phase of $Si_{1-x}Ge_x$ with the value 0 corresponding to the liquid phase and the value 1 identifying the crystal phase, (d) alloy fraction (X_{Ge}).*

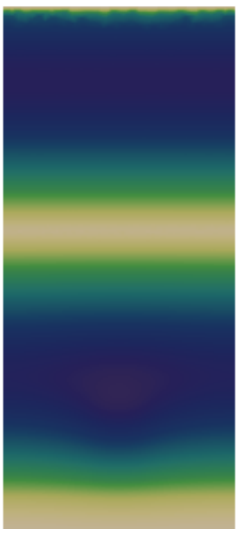

Figure 4.3. *Electromagnetic field module captured at 110 ns. The color legend is the same of Figure 4.2a.*

Table 4.1. *Melt threshold (ED Thr.) vs structural parameters for the various simulated $Si_{1-x}Ge_x$ patterned structures.*

Melt Thresholds vs Structural Parameters				
X	**Pulse [ns]**	**P [nm]**	**W [nm]**	**ED Thr. [J cm^{-2}]**
0.2	160	120	-	0.45
0.2	160	120	30	0.40
0.2	160	120	80	0.40
0.2	160	200	-	0.50
0.2	160	200	30	0.45
0.2	160	200	80	0.35
0.5	160	120	-	0.40
0.5	160	120	30	0.30
0.5	160	120	80	0.30
0.5	160	200	-	0.40
0.5	160	200	30	0.35
0.5	160	200	80	0.25

The analysis of different polarization angles, considering the prototypical case of X_{Ge}= 0.2, W = 30 nm, P = 120 nm, reported in Figure 4.4, shows slight variation on melting thresholds and MDs for ED = 0.8 J cm^{-2}. Moving from a polarization angle, θ, of 0° to 90°, ED threshold increases from 0.40 J cm^{-2} to 0.45 J cm^{-2}, while the MD of the aforementioned cases decreases from ~ 60 nm to ~ 45 nm.

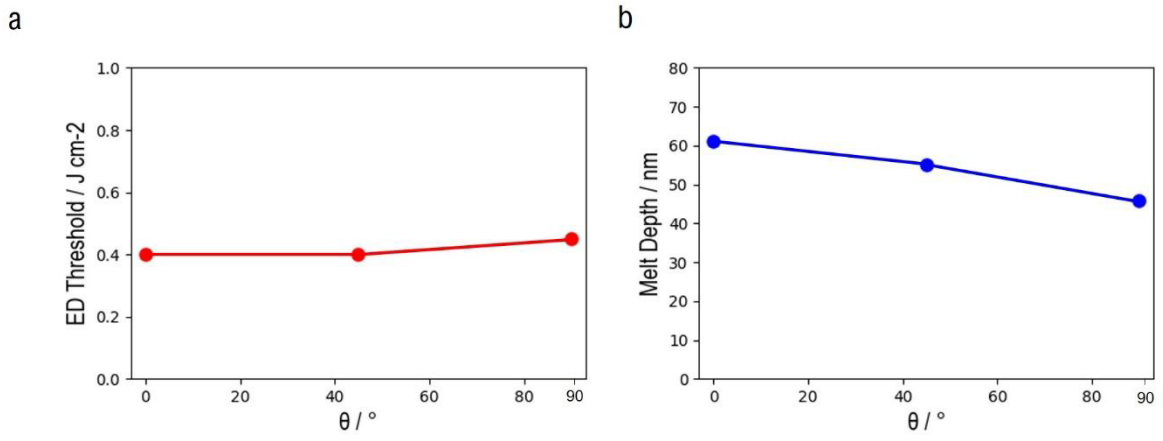

Figure 4.4. *Effect of laser polarization angle (θ) on melt threshold (ED threshold) (a) and melt depth (b). Simulations are performed for the case X = 0.2, P = 30 nm, W = 120 nm. The MDs are evaluated using an ED = 0.8 J cm^{-2}.*

5. Conclusions

We presented a functioning model for the process of melting and alloy redistribution of $Si_{1-x}Ge_x$. We addressed the issues related to the calibration, where a correct definition of the dielectric functions of l-$Si_{1-x}Ge_x$ was still missing. We calibrated those functions with an indirect approach, employing data of relaxed samples from the second round of experiments. We found that the resulting models yield accurate results also for strained samples with a good reproduction of melt depths (MDs) and of alloy redistributed profiles.

We extended our study to the modeling of $Si_{1-x}Ge_x$ pattern structures with simplified two-dimensional (2D) approaches. We found melting thresholds on average of 0.40 J cm^{-2} slightly tuned by the structural parameters, i.e., the width (W) of the SiO_2 capping layer and the pitch. We further investigated the variation of polarization angle, finding that when moving from 0° to 90°, the melt threshold slightly increases and the MD decreases, with an anti-reflectivity behavior. These predictions can be used as guidelines to assess the fluence process window in planned irradiation experiments based on fabricated patterned relaxed $Si_{1-x}Ge_x$ samples. The general finding is a patterning dependent process window while the alloy redistribution should not show a real 2D profile for all the cases considered in the Design of Experiments (DoE), due to the capillarity effect. The validation study of these simulation results will be part of the final activities of the MUNDFAB project.

References

1. La Magna, A., et al., *A phase-field approach to the simulation of the excimer laser annealing process in Si.* J. Appl. Phys., 2004. **95**(9): p. 4806-4814.
2. Lombardo, S.F., et al., *Theoretical study of the laser annealing process in FinFET structures.* Appl. Surf. Sci., 2019. **467-468**: p. 666-672.
3. Lombardo, S.F., et al., *Laser annealing in Si and Ge: Anomalous physical aspects and modeling approaches.* Mater. Sci. in Semicond. Process., 2017. **62**: p. 80-91.
4. Wagner, M., et al., *Power Output Improvement of Silicon-Germanium Thermoelectric Generators.* ECS Transactions, 2006. **3**(7): p. 1151.
5. Černý, R., et al., *Determination of the reflectivity of liquid semiconductors over a wide temperature range.* Int. J. Thermophysics, 1995. **16**(3): p. 841-849.
6. Abrahám, A. et al., *Optical Properties of Liquid Germanium.* physica status solidi (b), 1963. **3**(4): p. 767-772.
7. Huet, K., et al., *Pulsed laser annealing for advanced technology nodes: Modeling and calibration.* Appl. Surf. Sci., 2020. **505**: p. 144470.
8. Calogero, G., et al., *Multiscale modeling of ultrafast melting phenomena.* npj Comput. Mater., 2022. **8**(1): p. 36.
9. Dagault, L., et al., *Investigation of recrystallization and stress relaxation in nanosecond laser annealed $Si_{1-x}Ge_x$/Si epilayers.* Appl. Surf. Sci., 2020. **527**: p. 146752.
10. Dagault, L., et al., *Impact of UV Nanosecond Laser Annealing on Composition and Strain of Undoped $Si_{0.8}Ge_{0.2}$ Epitaxial Layers.* ECS J. Solid State Sci. Tech., 2019. **8**(3): p. P202.